NASA-TM-111252

AIAA–95–1862
Flowfield and Acoustic Characteristics of Telescope Cavity in SOFIA Platform

G. R. Srinivasan
Sterling Software
NASA Ames Research Center
Moffett Field, CA 94035–1000

AIAA 13th Applied Aerodynamics Conference
June 19–22, 1995 / San Diego, California

AIAA-95-1862-CP

FLOWFIELD AND ACOUSTIC CHARACTERISTICS OF TELESCOPE CAVITY IN SOFIA PLATFORM

G. R. Srinivasan*
NASA Ames Research Center, Moffett Field, CA 94035-1000

Abstract

Unsteady three-dimensional flowfields are calculated for the Stratospheric Observatory For Infrared Astronomy (SOFIA) at both free-flight cruise and wind tunnel conditions with a view to help in the design process of an acoustically quiet telescope cavity and to understand the flow physics of a three-dimensional cavity. The calculation method is based on the numerical solution of thin layer Navier-Stokes equations on a Chimera overset grid system. The Boeing 747-200 aircraft is examined as one option for the SOFIA platform. The flowfield domain is composed of 45 grids consisting of over 4.1 million points. Numerical simulations are performed for both wind tunnel and free-flight cruise conditions at one free-stream condition of $M_\infty = 0.85$, $\alpha = 2.5°$. Comparison of results from wind tunnel simulation show good agreement with experimental data for time-averaged surface pressures, drag for the empennage, and sound pressure levels and power spectra at various locations within the cavity and on the telescope. The presence of the open cavity induces an incremental drag increase, an increased acoustic radiation, and an increase in unsteady pressure loads on the telescope. Its impact on the effectiveness of aircraft control surfaces appears minimal.

Introduction

The SOFIA is a planned 2.5 meter aperture Cassegrain telescope with a Nasmyth focus, which will be housed in a Boeing 747 aircraft, and will operate at altitudes from 41,000 to 46,000 feet. It will be a follow-on mission to the NASA's Kuiper Airborne Observatory (KAO). The use of an airborne observation telescope housed in a moving platform, shown in an artist's view of Fig. 1, offers many advantages over a land-based system. In particular, the attenuation and/or absorption of wavelengths of interest by the water vapor in the earth's atmosphere will be avoided by using a system placed above the tropopause. However, the moving aircraft-based observatory poses problems of a different nature. As noted in earlier studies with a Boeing 747-SP configuration by Atwood,[1] the telescope-housing cavity poses a complex unsteady fluid dynamic problem that is difficult to control. Namely, experimental observations have shown violent shear layer oscillations accompanied by dangerous levels of noise. The high levels of turbulence in the unsteady shear layer would limit clear see-through vision of the telescope and hence decreases the capability of the telescope, in the absence of any flow control in the cavity to decrease flow unsteadiness. Besides the telescope seeing quality, the aircraft fatigue life and the control surface effectiveness are also affected by the flow unsteadiness of a resonant cavity.

There have been many experimental and computational investigations in the literature on the driven cavity problem[2]. In the last few years, extensive experimental testing has been done on the design of a non-resonant cavity for the telescope in the SOFIA platform using both Boeing 747-SP and 747-200 aircraft models.[3–5] The primary goal of these investigations was to identify a shear layer control scheme that provides lowest possible sound pressure levels (SPL) in the cavity and a non-resonant cavity environment. Computational investigations were also conducted by Atwood[6,7] using a sting mounted Boeing 747-SP aircraft wind tunnel model containing a telescope mounted in a separate forward and aft located cavity. A summary of the results from these investigations is described by Machak et al.[8]

The presence of an open cavity in an aircraft produces flow unsteadiness, increased drag penalty, and may alter aircraft stability and control. Further, the oscillating unsteady shear layer on the open cavity will affect the seeing ability of the telescope because of the increased density fluctuations in the shear layer. The impact of these effects and the effect of unsteady loads and moments on the telescope are briefly discussed in Ref. 8. There is a continuing emphasis on pursuing parallel experimental and computational efforts to arrive at a final configuration for the cavity, its aperture, and finally the telescope itself. The present investigation is one such study in this direction to evaluate the feasibility of using a Boeing 747-200 aircraft as an alternate configuration for the SOFIA platform. This computational investigation is the first one

* Sterling Software, Associate Fellow AIAA.

for the Boeing 747-200 as a platform but will complement the investigations of Atwood[6,7] and Klotz[8] done with the Boeing 747-SP aircraft. The location of the cavity, its proximity to the empennage surface, and the difference in the geometries of the two aircrafts will bring out similarities and/or differences of the impact of cavity flow between the two airborne platform concepts.

Numerical Method

The investigation of the aerodynamic issues pertinent to the SOFIA design has progressed along parallel paths using wind tunnel testing and computational simulations. The Computational Fluid Dynamic (CFD) simulations not only complement the experimental program but will provide a database that is hard to measure in a wind tunnel test. The numerical method solves the Reynolds averaged Navier-Stokes equations in thin layer form on an overset grid framework using the flow solver OVERFLOW.[9] This flow solver uses a central-differenced, implicit, diagonal algorithm[10] with added second- and fourth-order numerical dissipation terms. The numerical scheme is second-order accurate in space and first-order accurate in time.

The Navier-Stokes equations are solved in a computational domain described by the generalized coordinate system (ξ, η, ζ, τ) where $\xi = \xi(x, y, z, t)$, etc., and $\tau = t$. Here (x, y, z, t) is the inertial coordinate system. The nondimensionalization of length, velocity, density, pressure, etc., are done using a characteristic length scale (unit length), free-steam sound speed (a_∞), free-stream density (ρ_∞), and free-stream pressure (p_∞). The flow on the entire configuration is assumed to be fully turbulent at the Reynolds number of interest and an algebraic turbulence model[11] is used to estimate the eddy viscosity. A no-slip boundary condition is specified at the wall with zero normal pressure gradient along with an adiabatic wall condition. To update the information exchange at the overset grid interface, a trilinear interpolation of the dependent variables is used. The computations are performed on the NAS and Eagle Cray C-90 supercomputers.

The gridding of 45 overset grids of the SOFIA platform is a tedious job. Initially, the surface grids were reconstructed from CAD data[12] using GRIDGEN2D[13] and S3D[14] CFD tools. In addition, special tools developed at NASA Ames for constructing collar grids and cap grids were also utilized. The final clean configuration has 29 overset surface grids. In addition, there are 4 plume grids for the engines and 5 wake grids for the wings and the horizontal and vertical tail sections. The engine pylons were not included in this configuration. The cavity and the telescope assembly[7] is represented by another 7 grids for a total of 45 grids. Figures 2 and 3 show the surface geometry and surface grid representation, respectively. Once all surface grids (with overlaps) are constructed to the accuracy needed, then structured volume grids on these individual surfaces are carefully constructed. Grids of O-O, C-O, and H-H topology have been constructed using the Hypgen grid generator.[15] There are over 2.7 million grid points for the clean configuration (without cavity and telescope) and over 4.1 million grid points for the configuration with cavity and telescope. Table 1 lists the overset grids used and their corresponding dimensions. The maximum dimensions along ξ, η, and ζ directions are denoted by $JMAX$, $KMAX$, and $LMAX$, respectively. The spacing of the first grid point from the surface in these grids varied from grid to grid and was between $2\text{x}10^{-5}$C to $5\text{x}10^{-5}$C, where C is the characteristic length scale for each surface, eg., it is the average diameter of fuselage for fuselage grid, mean aerodynamic chord of wing for the wing grid, etc.

Once the grids are in place, the next step is to cut proper hole boundaries within the overset grids. This is achieved by running the PEGSUS code.[16,17] This is an iterative process and requires several iterations of hole punching and grid generation to eliminate all *orphan* points in the flowfield. Figure 4 shows one view of the hole boundaries in the Chimera grids for the clean aircraft generated by the PEGSUS code. The hole cutting job is a necessary step in the solution process as this hole boundary information is required to run the flow solver.

Results and Discussion

Numerical results of two CFD simulations, one corresponding to the full configuration free-flight (F-F) condition and the other to the wind tunnel (W-T) condition, are presented. Both these simulations are performed for a free-stream Mach number of $M_\infty = 0.85$, and an angle of attack at cruise of $\alpha = 2.5°$. The free-flight condition corresponds to cruise at 41,000 ft. altitude with powered engines (power setting is done via boundary condition procedure) and the appropriate Reynolds number at this altitude for the full-scale aircraft is $Re = 1.55$ million/ft. (The CFD simulation for the 7% scale model uses a value of $Re = 22.2$ million/ft. for free-flight condition.) The geometry of the aircraft for simulation at cruise is shown in Fig. 2.

The wind tunnel model used a slightly different configuration from the free-flight case. The wind tunnel model has no engines and its wings are clipped (for smaller aspect ratio) to accomodate the model in

the 14-Foot Wind Tunnel of NASA Ames Research Center. Figure 5 shows a view of the wind tunnel model with an aft located cavity and telescope. Figure 6 shows the surface grids of the cavity and the telescope used in these simulations. The flow Mach number and angle of attack are the same as the free-flight conditions but the Reynolds number of the wind tunnel test is 4 million/ft.

The location of the telescope cavity and its geometry, including its nearly circular aperture, are same for the two CFD simulations. The aperture has a smooth aft ramp downstream of the cavity as shown in Figs. 5 and 6. The telescope geometry, shown in Fig. 6, is a simplified version of the actual telescope used in the wind tunnel model shown in Fig. 5.

In obtaining the unsteady solutions, first steady state solutions of the clean aircraft and the aircraft with cavity are calculated. A variable time-step option was used to accelerate the convergence to steady state. The solution was assumed to have reached steady state after the L_2-Norm in all the grids has dropped by about 3.5 - 4.0 orders of magnitude. Figures 7 and 8 show comparisons of surface pressure coefficients (C_p) on the wing and fuselage calculated for free-flight cruise and scaled to wind tunnel condition with experiments.[18] Although experimental conditions did not match exactly with the conditions of the CFD simulations, the comparisons shown in Figs. 7 and 8, nevertheless, provide a guideline to the trends and accuracy of the CFD simulations. For example, the comparison of surface pressures on the wing (Fig. 7) show that the data measured at M_∞ = 0.86 and $\alpha = 3°$ has better agreement with CFD results than the one measured at $M_\infty = 0.84$ and at the same angle of attack, suggesting that there may have been some blockage effect in the wind tunnel data. Overall, the agreement with experiments at $M_\infty = 0.86$ is very good, including the location and strength of shocks on the wing. The results in Fig. 8 are compared with a different set of experimental data supplied by the Boeing Airplane Company[18] and therefore the experimental conditions are slightly different. Also, the experimental data is measured on a sting mounted model that did not have an empennage. The comparison of the nose to tail surface pressures on the fuselage at three representative azimuthal locations along its length show good agreement with experiments, at least over the region that excludes the empennage surface.

Unsteady calculations were run starting from steady solutions. These calculations were run with a constant nondimensional time-step of 0.11, which translates to 136 microseconds of real-time for F-F condition and 9.5 microseconds for W-T condition. The unsteady data was accumulated only after the initial transients were completely eliminated. A 1.5 second real-time data trace was accumulated for the free-flight calculation and a 0.13 second real-time data trace was accumulated for the wind tunnel calculation. A typical calculation like this took over 120 Cray-90 CPU hours that included the initial steady solution.

Figure 9 shows a comparison of wind tunnel simulation and experimental time-averaged surface pressure coefficients (C_p) for the empennage surface. Comparisons are presented for both portside horizontal tail and vertical tail. The results show very good agreement with experiments for some stations, and small discrepancies for others. Nevertheless, it should be noted that the results from experiments are time-averaged over a 5 second real-time trace compared to a small fraction of such a time trace for the computations. Despite this difference, the good agreement of surface pressures is very impressive. Figure 10 shows a snapshot picture of the unsteady surface pressures (C_p) for the full aircraft at free-flight cruise condition. The surface color map shows a variation of C_p according to the noted color scale, with red indicating high pressures and blue for low pressures. The cavity aft bulkhead region is seen as a region of high pressure followed by a small flow expansion region on the ramp of the cavity aperture.

Figure 11 presents for the wind tunnel simulation, the computed unsteady pressure history, $(p(t)/p_\infty)$, and power spectral density (PSD) plots for two locations on the forward bulkhead surface identified in the figure in Table 2. The spectra were computed from a record containing 1923 data points and zero-padded to 2048 points. The data points were stored in the computations at regular 25 time-steps intervals. Welch windowing function[19] is applied to compute the spectra. Although other windowing functions, such as Hann, Parzen, and Bartlett, are available, Atwood[6] has shown that Welch windowing is more appropriate for the SOFIA cavity environment.

The results presented in Fig. 11 show that there are some differences in the surface pressure histories, but their spectra is largely similar, particularly in the frequency range between 400 Hz to 1400 Hz. The spectra shows a rapid fall-off at high frequencies due to inadequate resolution of high frequency waves. At the low frequency end, the spectra is not well resolved due mainly to the brevity of the length of data trace accumulated in the simulation. Table 2 lists the energy contained in these spectra in the form of sound pressure levels (SPL) calculated at specified locations for both wind tunnel and free-flight conditions. The experimental data is available for the location 49 shown in this Table. The SPL at this point

from measurements is about 11 dB more than what W-T CFD predictions show. Although it is hard to pin the exact reason for this difference, it should be noted that small differences in the geometry might contribute to such differences. However, the CFD results at W-T conditions scaled to F-F show a fair comparison with F-F CFD results. Some locations show much larger disagreement than others. It is important to mention that the scaling laws used accounts for the change in free-stream conditions and length scale, but the difference in boundary layer behavior is accounted for only through the Reynolds number scaling, which may be inadequate.

Similarly, Fig. 12 presents the unsteady pressure histories and PSD for the aft bulkhead surface locations shown in Table 3. The locations identified by points 53 and 54 show almost identical behavior for surface pressure histories and PSD. Although location 55 shows a slightly different surface pressure history, its spectra (not shown here for clarity of the figure) is similar to that of points 53 and 54. The spectra identifies several characteristic frequency that are important for this cavity. The calculated SPL are listed in Table 3 along with experimental value at locations 53 and 54. Although not in perfect agreement, the CFD predictions show a better agreement with experiments for this aft bulkhead surface than the comparisons of the forward bulkhead surface SPL.

A comparison of PSD from the W-T CFD simulation and experiment are shown in Fig. 13 for the bulkheads at the indicated locations. Two sets of experimental data are shown in Fig. 13 that were measured on two different but nearly identical configurations. In all the cases where the spectra is compared with experimentally determined spectra, the experimental spectra are calculated from a five seconds long data trace compared to a 0.13 seconds trace for the CFD simulation. In spite of this disparity, the level of spectra from the CFD simulation compares well with experimental data in the 400 Hz to 1400 Hz range. Below that range of frequency the CFD simulation is affected by the brevity of the simulation time-trace and above that range numerical disspation causes a rapid fall-off of the spectrum, as mentioned before. Even though the levels of spectra are below that of experiment, the dominant frequencies (the peaks in spectra) are well captured, particularly at 400 Hz and 1100 Hz, and are in agreement with experiment.

Figure 14 shows a plot of power spectra at a point of interest on the cavity aperture at location AP1 (see the figure in Table 5) calculated for full configuration F-F condition and scaled to W-T condition and compared with other data. As seen, the present calculations for the Boeing 747-200 platform are compared with CFD results for the Boeing 747-SP platform with and without the empennage and with the experiments.[20] Atwood[6] computed flowfields on a sting-mounted 747-SP wind tunnel model of Rose and Cooley[20] that had cavities located forward and aft of the wing. Klotz,[21] on the other hand, used the 747-SP platform with an empennage and also had the aft-located (downstream of wing) cavity in his simulations. The comparisons show that the spectra from all the above CFD simulations at this point on the cavity aperture have similar behaviors. The level of spectra from the present simulations for the 747-200 is slightly lower than for the 747-SP configuration and the experiment of Rose and Cooley.[20] This indicates that the SPL at this location is lower for the 747-200 platform compared to the 747-SP platform, even though the cavity and aperture shape and size are identical. The proximity of the cavity to the empennage surface for the two configurations is different; the cavity is much farther located from the empennage for the 747-200 platform than the 747-SP platform. As before, the CFD simulations show a much more rapid fall-off of spectra compared to experiments. Table 4 presents the calculated SPL for different locations on the aperture surface. As observed for bulkheads, the sound pressure levels calculated from W-T simulations and scaled to F-F show consistently higher values compared to the values determined from F-F simulations.

Figures 15-22 present the data for the telescope. The unsteady pressure history computed for the W-T case is presented in Fig. 15 for locations shown in Table 5 on the primary mirror and telescope tub. The pressures on the bottom of the telescope tub show very little variation from each other in time compared to the points on the primary mirror. This is because the telescope tub is immersed in a region of recirculating, relatively low speed flow. The power spectra for these same locations are presented in Figs. 16 and 17 along with the results from F-F simulations. As seen, the spectra computed from F-F simulations show distinct dominant frequencies in the range of 400 Hz to 1400 Hz. The W-T simulations also show distinct frequencies that are dominant, but they are not as pronounced as seen from the F-F simulation in the same frequency range, viz., the 400 Hz and 1200 Hz seen in Figs. 16b and 17b.

A comparison of PSD from the W-T simulation with experiment is shown in Fig. 18 for locations for both the primary mirror and the telescope tub. As noted before, the spectra determined from computations falls-off much faster than indicated by experiments. The overall levels of CFD prediction are below that of the experiment, but the dominant peaks in the spectrum are well captured, particularly the ones around 400 Hz and 1100 Hz. The sound pressure levels for these two surfaces are tabulated in Table 5.

As seen in this Table, the SPL on the primary mirror compare well with the CFD W-T values, but the region of telescope tub shows the SPL's to be underpredicted, perhaps due to the simplified tub geometry used in the computational simulations. Comparison of W-T CFD results scaled to F-F with that from the F-F CFD simulation shows generally a good agreement for the primary mirror, but the bottom of the tub shows at least a 10 dB difference at each point for the two simulations.

Time histories of unsteady force coefficients on the telescope are presented in Fig. 19 for W-T and F-F simulations. The OVERFLOW code uses the free-stream sound speed as the velocity scale. But the force and moment coefficients use standard definition of dynamic pressure, viz., $0.5\rho_\infty\ {u_\infty}^2$, where ρ_∞ and u_∞ are the free stream density and velocity, respectively. The scaled (dimensional) values of lift, drag, and side force on the telescope are tabulated in Table 6. The lift, drag, and side force on the telescope are components of force in the aircraft frame of reference. As seen from the time histories of force coefficients in Fig. 19 and the magnitude of mean loads, the lift and drag values are in good agreement from the two simulations. The drag for telescope is negative, consistent with the fact that the pressure on the aft bulkhead is higher than the rest of the cavity pressure. The F-F calculations show a value for side force approximately half of what is calculated from the W-T simulation. The reason for this discrepancy is not clear at the present time. Examination of unsteady force coefficients in Fig. 19 shows that the behavior of side force coefficient time-history trace is not consistent with those of lift and drag traces. Also, inspection of computed forces from Table 6 shows the mean values of lift and drag forces to be in agreement for the two simulations. The side force from the W-T simulation, on the other hand, is about 2.5 times the value from the F-F simulation. This difference in forces between the two simulations has also produced differences in the rolling and yawing moments.

The moment coefficients on the telescope about the aircraft axis are presented in Fig. 20. The scaled values of mean and root mean square (rms) values of pitching (Pm-Air B), rolling (Rm-Air B), and yawing (Ym-Air B) moments, about the telescope air bearing are tabulated in Table 6. Also tabulated in this are the moments about an axis system that is of interest to the SOFIA Project Office. The scaled moments, viz., moment about the telescope cross-elevation axis (Tmom-CEle axis), moment about the telescope line-of-sight axis (Tmom-LOS axis), and moment about the telescope elevation axis (Tmom-Ele axis) are referenced with respect to the coordinate axes, which are parallel to the aircraft axes when the telescope is at 90° elevation angle, 0° LOS, and 0° cross-elevation and pass through the center of the telescope air bearing (origin of telescope coordinate system) shown in Fig. 21. The air bearing assembly, mounted forward of the instrument in the aircraft, supports the telescope. The air bearing assembly isolates the telescope bay from the pressurized sections of the aircraft and supports all loads on the telescope. The center of the air bearing is located on the y = 0 symmetry plane, 10 in. forward of the forward bulkhead of the cavity and 6 in. above the longitudinal axis of fuselage.

The mean and rms values of moments on the telescope for both F-F and W-T conditions are presented in Table 6. The W-T CFD values of loads and moments are scaled to the F-F condition to compare directly with F-F CFD simulation. Inspection of these results reveals the mean values of moments from the two simulations to be in agreement only in order-of-magnitude. The two results differ in magnitude by as much as a factor of 2. The telescope moment about the cross-elevation axis (Tmom-CEle axis) from the wind tunnel simulation scaled to F-F condition is -699 ± 145 ft-lb and the measured value of the same quantity from the wind tunnel test[22] scaled to F-F condition is -378 ± 692 ft-lb. The magnitude of this moment from the F-F simulation is -290 ± 534 ft-lb. Considering that there are some differences in the telescope geometry for the W-T experimental model and the CFD simulations, the F-F result shows good agreement with the measured value for this telescope moment. The W-T simulation, on the other hand, gives a value that is about twice the experimental and the F-F CFD results for the same telescope moment. It appears that over prediction of telescope side force from W-T simulation is directly producing the differences in the various moments calculated from these forces. The brevity of the CFD time-trace for the W-T simulation cannot be the reason for the difference with the F-F simulation result as the length of time-traces for the two simulations are nearly same in the wind tunnel scale.

The power spectra of the telescope moment about cross-elevation axis calculated from W-T simulation is compared to wind tunnel experiment in Fig. 22. The F-F CFD result of spectra, scaled to the W-T condition, is also presented in this plot. The comparison shows that the two CFD results give nearly identical spectra. They both agree well with experimental data in the frequency range of 300 Hz to 1200 Hz. The peaks in the spectra are well captured by CFD simulations and agree well with experiments, but the level of the spectra in the CFD predictions is slightly underpredicted. As mentioned before, the CFD results are affected by the brevity of the simulation duration

and hence lack resolution in the low frequency end of the spectra. At higher frequencies exceeding 1200 Hz, the CFD results have a steep fall-off due to inadequate resolution of high frequency waves by the numerical scheme. Nevertheless, the dominant frequencies shown in the experimental spectra are well captured by both CFD simulations in the frequency range of 300-1200 Hz although the level of spectra is underpredicted.

Accurate determination of drag force from CFD simulations is subjected to uncertainties in gridding, turbulence model, and complexity of the geometry. This is particularly true when one is using a large number of overset grids. Until now there were no CFD tools available to estimate drag in the regions of grid overlap in overset grids. Chan and Buning[23] have recently developed a method to construct *zipper* grids on the surface of the body in the regions of grid overlaps in a multigrid system. In essence, the method locates the overlap region and generates a composite surface grid consisting of non-overlapping quadrilaterals and triangles.

Using this method, zipper grids were constructed for all overlap regions in the present 45 overset grid system. Figure 23 shows a composite view of the aircraft with zipper grids constructed in the grid overlap regions. These can be seen as color patches in several overlap regions on the surface, for example at tips of wings and the empennage, collar grids, cavity, etc. Typical zipper grids are shown for the engine at the junction of nacelle-fan and fan-core in Fig. 23. Using the information of new surfaces, force coefficients are then determined. The calculated drag coefficients are tabulated for different components of the aircraft in Table 7. The drag coefficient has in it the pressure and skin friction components. Drag coefficients for clean aircraft and that with cavity are listed separately. From these results, the incremental drag coefficient due to the presence of the cavity for W-T simulation is 0.000063, whereas the incremental drag for F-F simulation is 0.000255. It should be noted that that the drag coefficient reported here uses $0.5\rho_\infty u_\infty^2$ for the dynamic pressure. The density and velocity correspond to the local free-stream conditions.

Also listed in Table 7 is the drag coefficient for the empennage only, which include the horizontal and vertical tails and the supporting part of the fuselage as shown in Fig. 9. The experimental determination of drag coefficient has been done by two independent methods.[8] The comparison of results from CFD simulation and experiment show very good agreement. The incremental drag on the empennage due to the cavity is 0.000056, which compares well with the result quoted above. The detailed determination of drag for individual components of the aircraft from the CFD simulation is a valuable piece of information and has been done here for the first time from CFD analysis.

Conclusions

Unsteady flowfield and acoustic information have been obtained by CFD simulation of the Boeing 747-200 aircraft which is a candidate platform for the SOFIA, which is a 2.5 meter aperture Cassegrain telescope with a Nasmyth focus. The numerical method solves the thin layer Navier-Stokes equations on an overset grid system containing over 4.1 million grid points. Calculations are done for both full configuration free-flight condition at 41,000 ft. altitude with powered engines as well as at wind tunnel conditions. This computational investigation complements a parallel experimental investigation underway at NASA Ames Research Center. Together, they aid in the understanding of the unsteady flow physics associated with cavity flows and will eventually help in the design process of an acoustically quiet telescope cavity with good seeing quality and mimimum impact on aircraft stability.

Numerical results are presented for the wind tunnel simulation and compared with wind tunnel data. In general, there is good agrement for time-averaged surface pressures, sound pressure levels, power spectra over a frequency range of 300-1200 Hz, loads on the telescope, and empennage drag. The wind tunnel CFD results are also scaled to free-flight cruise conditions and compared with F-F CFD results. Although, there is general agreement between the two results, the sound pressure levels for W-T scaled results are generally higher than the F-F results and the experimental sound pressure levels are consistently higher by about 4-8 dB from W-T CFD results.

The presence of an aft located cavity for telescope does not seem to be detrimental to the control surface effectiveness and the stability of the aircraft.

Acknowledgements

The valuable help given by Dr. Chris Atwood in the begining stages of this project is greatly appreciated. Helpful discussions with Dr. Steve Klotz and Mr. Danny Machak are also appreciated.

References

1. Atwood, C. A., "Navier-Stokes Simulations of Unsteady Transonic Flow Phenomena," NASA Technical Memorandum 103962, August 1992.

2. Komerath, N. M., Ahuja, K. K., and Chambers, F. W., "Prediction and Measurement of Flows over Cavities - A Survey," AIAA Paper 87-0166, Jan. 1987.

3. Rose Engineering Research, Inc., "SOFIA Wind Tunnel Data Analysis and Implications for Full-Scale SOFIA Aircraft," Dec. 1990, (unpublished).

4. Rose Engineering Research, Inc., "SOFIA - Aft Cavities Wind Tunnel Test, Pre-test Report", Feb. 1993, (unpublished).

5. Rose Engineering Research, Inc., "SOFIA Wind Tunnel Test Monthly Reports, May - October 1993, June - August 1994," (unpublished).

6. Atwood, C. A. and Van Dalsem, W. R., "Flowfield Simulation About the Statospheric Observatory for Infrared Astronomy," *Journal of Aircraft*, Vol. 30, No. 5, 1993, pp. 719-727.

7. Atwood, C. A., "Unsteady Fluid and Optical Flow Simulation of Transonic Aero-Windows," AIAA Paper 93-3017, July 1993.

8. Machak, D., Srinivasan, G. R., and Klotz, S. P., "Aerodynamic Characteristics of the Stratospheric Observatory for Infrared Astronomy," AIAA Paper 95-0398, Jan. 1995.

9. Buning, P. G. and Chan, W. M., "OVERFLOW User's Manual, Version 1.6al," NASA Ames Research Center, July 1994, (unpublished).

10. Pulliam, T. H. and Chaussee, D. S., "A Diagonal Form of an Implicit Approximate-Factorization Algorithm," *J. Comp. Phys.*, Vol. 39, Feb. 1981, pp. 347-363.

11. Baldwin, B. S. and Lomax, H., "Thin-Layer Approximation and Algebraic Model for Separated Turbulent Flows," AIAA Paper 78-257, Jan. 1978.

12. Wigton, L., Private Communication, The Boeing Company, Aug. 1993.

13. Steinbrenner, J. P., Chawner, J. R., and Fouts, C. L., "A Structured Approach to Interactive Multiple Block Grid Generation," AGARD FDP Specialists Meeting on Mesh Generation for Complex Three-Dimensional Configurations, Loen, Norway, May 1989.

14. Luh, R. C.-C., Pierce, L. E., and Yip, D., "Interactive Surface Grid Generation," AIAA Paper 91-0796, Jan. 1991.

15. Chan, W. M. and Steger, J. L., "A Generalized Scheme for Three-Dimensional Hyperbolic Grid Generation," AIAA Ppaer 91-1588, June 1991.

16. Benek, J. A., Buning, P. G., and Steger., "A 3-D Chimera Grid Embedding Technique," AIAA Paper 85-1523, July 1985.

17. Suhs, N. E., and Tramel, R. W., "PEGSUS 4.0 User's Manual," AEDC-TR-91, June 1991.

18. Tinoco, E. N. and Yu, N. J., Private Communication, The Boeing Company, Seattle, Washington, Jan. 1994.

19. Press, W. H., Teukolsky, S. A., Vetterling, W. T., and Flannery, B. P., *Numerical Recipies in FORTRAN*, 2nd Ed., Cambridge University Press, Cambridge, U. K., 1992.

20. Rose, W. C. and Cooley, J. M., "SOFIA Wind Tunnel Data Analysis and Implications for the Full-Scale Aircraft," Rose Engineering and Research, Inc. Tech. Report, December 1990, (unpublished).

21. Klotz, S. P., "Numerical Simulation of the SOFIA Flowfield," MCAT Institute Annual Report submitted to NASA Ames Research Center, July 1994.

22. Keas, P., "SOFIA II Model Telescope Wind Tunnel Test," SVERDRUP, NASA Ames Research Center, Dec. 1994, (unpublished).

23. Chan, W. M. and Buning, P., "Zipper Grids for Force and Moment Computation on Overset Grids," AIAA Paper 95-1681, June 1995.

Table1: Overset grid system

Grid no.	Name	JMAX × KMAX × LMAX
1 2	Fuselage { Port side Starboard side	151 × 63 × 61*
3 4	Wing { Port side Starboard side	109 × 35 × 61
5 6	Wing tip cap { Port side Starboard side	31 × 21 × 45
7 8	Wingroot collar { Port side Starboard side	137 × 21 × 31
9 10	Wing wake { Port side Starboard side	31 × 71 × 41
11 12	Port side Engine nacelle { Inboard Outboard	88 × 17 × 45
13 14	Port side Engine fan { Inboard Outboard	15 × 17 × 31
15 16	Port side Engine core { Inboard Outboard	15 × 17 × 31
17 18	Port side Engine plume { Inboard Outboard	61 × 17 × 35
19 20	Starboard side Engine nacelle { Inboard Outboard	88 × 17 × 45
21 22	Starboard side Engine fan { Inboard Outboard	15 × 17 × 31
23 24	Starboard side Engine core { Inboard Outboard	15 × 17 × 31
25 26	Starboard side Engine plume { Inboard Outboard	61 × 17 × 35
27 28	Horizontal tail { Port side Starboard side	67 × 17 × 35
29 30	Horizontal tail tipcap { Port side Starboard side	21 × 31 × 43
31 32	Horizontal tail root collar { Port side Starboard side	57 × 13 × 41
33 34	Horizontal tail wake { Port side Starboard side	19 × 21 × 31
35	Vertical tail	61 × 18 × 45
36	Vertical tail tipcap	21 × 21 × 45
37	Vertical tail root collar	65 × 14 × 45
38	Vertical tail wake	18 × 14 × 21
39	Cavity aperture	52 × 175 × 37
40	Cavity aft bulkhead	33 × 125 × 41
41	Cavity forward bulkhead	31 × 125 × 37
42	Cavity inskin	41 × 111 × 37
43	Shear layer	61 × 61 × 91
44	Telescope	73 × 75 × 37
45	Secondary mirror	25 × 21 × 29

*Port side and starboard side grids have identical dimensions.

Table 2: SPL on forward bulkhead surface

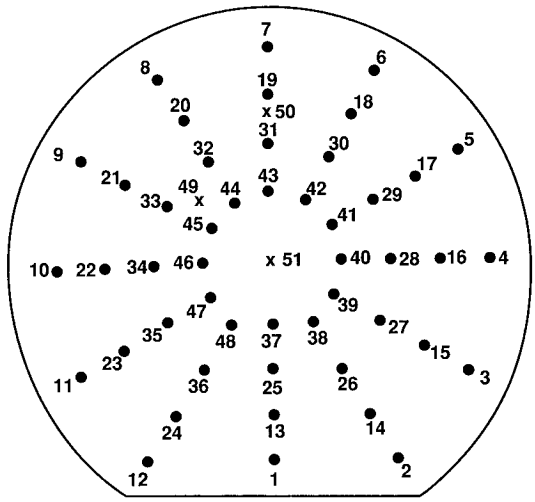

Location	SPL at W-T condition		SPL at F-F condition	
	CFD result	Experiment	W-T CFD result scaled to F-F	F-F CFD result
1	132.98		121.52	113.89
2	130.59		119.12	114.05
3	134.27		122.81	115.60
4	135.76		124.29	124.46
5	139.09		127.63	117.80
6	129.83		118.37	117.05
7	128.06		116.60	115.82
8	126.84		115.38	111.65
9	129.68		118.22	113.78
10	129.69		118.23	116.81
11	130.59		119.12	112.78
12	131.86		120.39	112.62
13	129.28		117.81	109.65
14	130.73		119.27	111.22
15	130.32		118.85	112.19
16	130.48		119.01	114.38
17	133.43		121.97	119.24
18	129.96		118.50	118.41
19	128.14		116.68	115.43
20	126.24		114.80	112.49
21	127.73		116.27	117.31
22	126.41		114.95	114.52
23	127.58		116.12	112.95
24	129.02		117.55	113.06
25	128.69		117.23	108.94
26	129.97		118.51	108.96
27	128.20		116.74	113.18
28	127.94		116.48	116.36
29	130.94		119.48	115.63
30	130.05		118.59	115.42
31	128.82		117.36	116.93
32	127.21		115.75	115.36
33	127.96		116.50	113.66
34	126.89		115.43	117.24
35	128.12		116.66	113.93
36	129.57		118.10	111.38
37	134.22		122.76	123.24
38	129.69		118.23	111.81
39	130.99		119.54	112.78
40	134.76		123.30	113.98
41	132.39		120.93	113.87
42	131.13		119.67	113.90
43	128.46		116.99	113.39
44	130.23		118.77	115.89
45	127.80		116.34	112.13
46	131.80		120.34	117.43
47	127.84		116.38	115.08
48	129.30		117.84	113.54
49	128.04	139.39		

Table 3: SPL on aft bulkhead surface

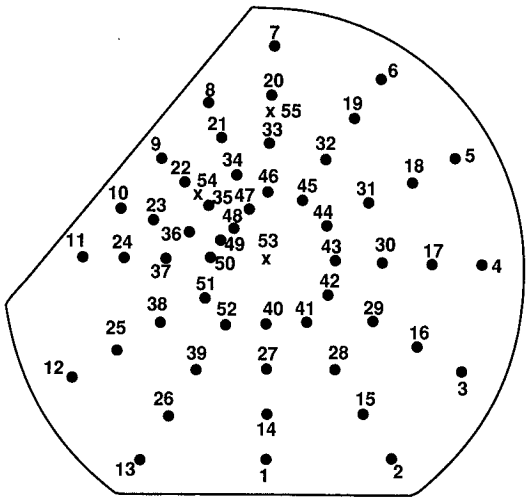

Location	SPL at W-T condition		SPL at F-F condition	
	CFD result	Experiment	W-T CFD result scaled to F-F	F-F CFD result
1	134.66		123.20	112.91
2	140.17		128.71	116.87
3	134.34		122.88	124.12
4	133.42		121.96	121.89
5	137.79		126.33	121.13
6	132.55		121.09	122.95
7	129.86		118.39	123.43
8	131.79		120.32	127.17
9	134.95		123.48	119.12
10	137.69		126.23	115.81
11	138.69		127.23	116.15
12	129.06		117.60	110.65
13	133.02		121.55	110.99
14	129.04		117.58	111.26
15	134.95		123.49	115.18
16	137.70		126.23	120.41
17	138.70		127.23	119.38
18	135.10		123.64	117.79
19	136.32		124.85	121.48
20	144.43		132.96	124.28
21	128.05		116.58	121.35
22	128.50		117.04	117.98
23	129.79		118.32	112.57
24	129.05		117.58	113.01
25	128.50		117.04	110.08
26	129.79		118.32	110.35
27	141.62		130.15	112.27
28	138.48		127.01	112.73
29	139.21		127.74	114.11
30	143.31		131.85	115.62
31	133.96		122.50	118.67
32	128.02		116.55	118.48
33	128.55		117.09	124.26
34	133.22		121.75	117.67
35	130.75		119.29	118.02
36	129.19		117.73	111.31
37	132.66		121.19	111.66
38	132.25		120.79	110.34
39	134.94		123.47	110.93
40	131.79		120.32	110.33
41	134.46		123.00	111.97
42	135.12		123.66	115.50
43	140.93		129.47	113.46
44	143.59		132.13	114.09
45	134.66		123.19	113.73
46	132.78		121.31	113.71
47	135.10		123.64	121.83
48	136.32		124.85	118.88
49	144.43		132.96	113.69
50	133.70		122.24	112.18
51	129.19		117.73	112.33
52	132.66		121.20	110.50
53	133.11	138.61		
54	134.79	137.38		

Table 4: SPL on aperture surface

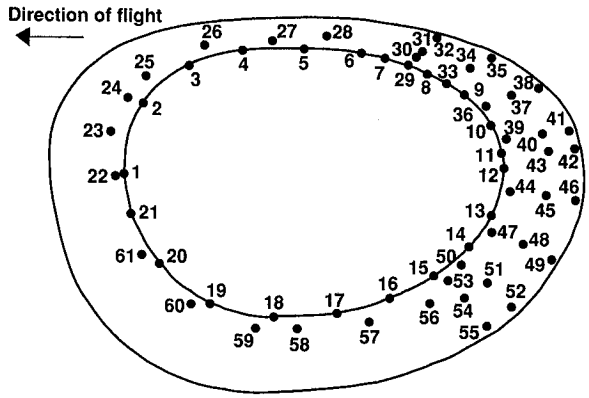

Location	SPL at F-F condition	SPL at W-Tcondition scaled to F-F
1	109.9276	118.7972
2	108.3877	116.7992
3	114.9997	120.1128
4	137.8785	142.3908
5	135.7606	141.8152
6	125.5751	134.0716
7	121.8111	131.1366
8	125.0713	128.3320
9	122.9297	125.1205
10	120.9662	129.8767
11	121.3782	132.1963
12	121.8336	131.9763
13	127.1875	132.0928
14	131.3654	134.0126
15	130.8833	135.0146
16	130.9776	133.1084
17	133.9267	137.7588
18	131.1858	138.4326
19	122.7684	131.3456
20	109.7654	129.4281
21	111.3941	127.2274
22	106.5218	114.4526
23	107.5705	113.8963
24	104.4546	112.2690
25	104.3805	112.2320
26	115.0066	119.4801
27	128.3355	133.4393
28	122.6311	128.8815
29	116.3789	116.0737
30	112.8542	121.9772
31	113.8103	119.1613
32	109.6358	114.6214
33	107.8794	109.9093
34	121.8192	124.2691
35	117.0359	120.8275
36	107.9717	113.1449
37	102.4701	113.4056
38	095.9949	106.6243
39	097.0809	113.8330
40	102.6626	110.4983
41	106.0777	110.0702
42	111.2880	115.6195
43	107.8962	112.4716
44	108.4878	112.8802
45	110.6609	115.0954
46	112.1135	116.1066
47	114.9250	119.6102
48	113.3975	116.2875
49	106.4596	114.9989
50	121.4133	128.4326
51	118.4583	128.6562
52	118.3532	123.3158
53	124.9123	129.6813
54	125.9247	128.3338
55	123.6237	128.4326
56	123.5605	125.7325
57	122.8858	126.8932
58	122.4498	128.4372
59	119.9573	126.6832
60	114.1938	121.8236
61	106.0902	121.7976

Table 5: SPL on telescope surface

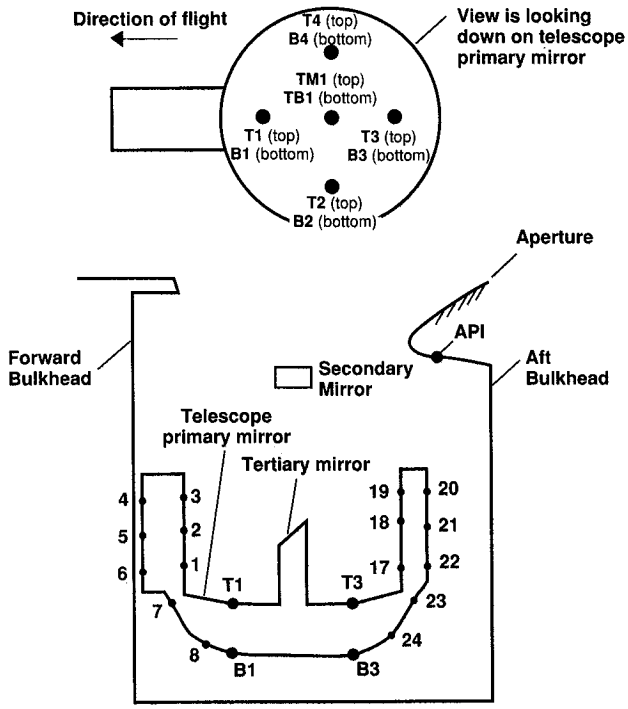

Location	SPL at W-T condition		SPL at F-F condition	
	CFD result	Experiment	W-T CFD result scaled to F-F	F-F CFD result
1			113.2862	114.2914
2			114.2390	114.4882
3			113.6758	114.3002
4			115.9236	112.0297
5			116.2265	113.7740
6			121.2730	114.2470
7			124.7855	110.2452
8			116.7548	111.3190
9			113.7010	117.5999
10			110.0789	112.8209
11			110.8614	111.9682
12			113.8498	108.2472
13			117.0872	109.7667
14			123.7555	112.0150
15			125.0933	113.3403
16			114.4449	114.8532
17			115.8335	115.9031
18			116.2809	115.0371
19			116.7689	117.4681
20			115.2234	115.1727
21			116.7408	115.6934
22			128.3664	114.4056
23			126.2504	113.5241
24			129.1852	111.8642
25			113.5956	123.9523
26			113.4152	118.3908
27			114.5594	126.5063
28			116.4477	116.1369
29			116.9713	115.8134
30			114.0912	116.8123
31			116.7548	112.8908
32			120.6173	116.4895
T1	127.9	135.5		
T2	137.7	135.0		
T3	136.0	130.9		
T4	131.5	134.8		
B1	126.3	133.1		
B2	127.1	133.2		
B3	127.1	133.8		
B4	126.5	133.3		

Table 6: Telescope loads and moments

Loads (lbf) and moments (ft-lb)	F-F CFD simulation	W-T CFD simulation scaled to F-F
Lift	28.49 ± 17.24	21.41 ± 6.43
Drag	-45.74 ± 12.94	-43.19 ± 21.40
Side force	22.34 ± 16.53	54.28 ± 38.39
Pm_Air B	459.4 ± 457.7	571.2 ± 234.5
Rm_Air B	-201.8 ± 25.9	-463.9 ± 286.8
Ym_Air B	764.5 ± 456.3	1738 ± 1089.4
Tmom_CEle axis	-290.35 ± 533.9	-698.6 ± 144.8
Tmom_Los axis	843.1 ± 374.9	463.9 ± 286.7
Tmom_Ele axis	201.8 ± 25.9	679.1 ± 214.5

Table 7: Drag coefficient – computed and experiment

Component	W-T case at W-T conditions		F-F case	
	Clean aircraft	Aircraft with cavity	Clean aircraft	Aircraft with cavity
Fuselage				
Portside	0.001525	0.001524	0.001015	0.001201
Starboard	0.001528	0.001529	0.001015	0.001020
Wing				
Portside	0.001386	0.001385	0.001120	0.001115
Starboard	0.001391	0.001393	0.001119	0.001118
Engines				
Portside			0.000481	0.000470
Starboard			0.000466	0.000465
Horizontal tail				
Portside	0.000084	0.000081	0.000033	0.000036
Starboard	0.000085	0.000081	0.000031	0.000032
Vertical tail	0.000388	0.000385	0.000248	0.000225
Telescope and secondary mirror	0.000000	-0.000010	0.000000	-0.000006
Cavity (5 grids)	0.000000	0.000062	0.000000	0.000060
Total C_D	0.006387	0.006450	0.005528	0.005783
Drag for empennage only for W-T model				
CFD Results	0.002095	0.002151		
Experimental Value	0.001979	0.001968		

Fig. 1: Artist's concept of the SOFIA configuration.

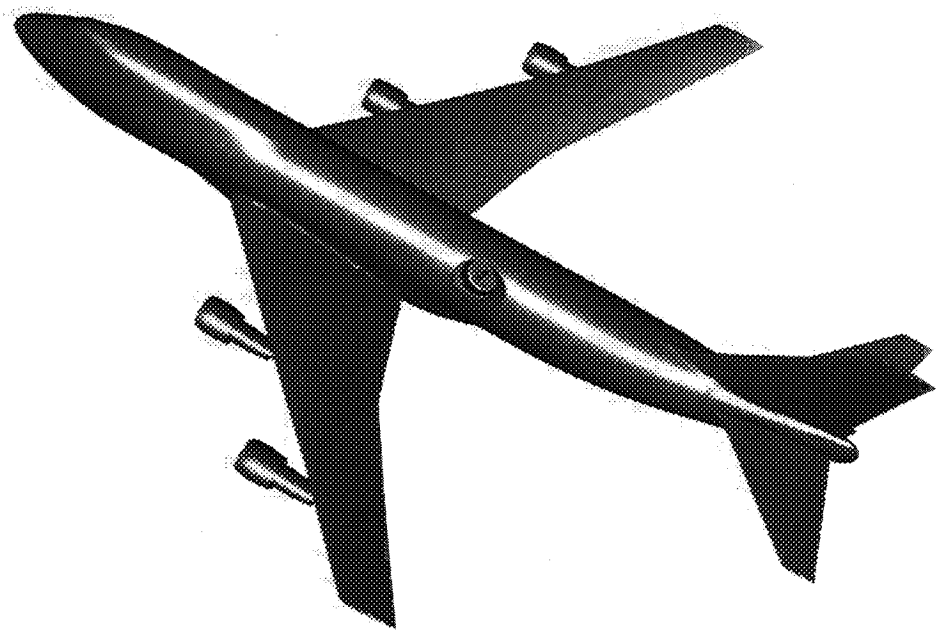

Fig. 2: Surface geometry of the Boeing 747-200 aircraft with an open cavity used in this study.

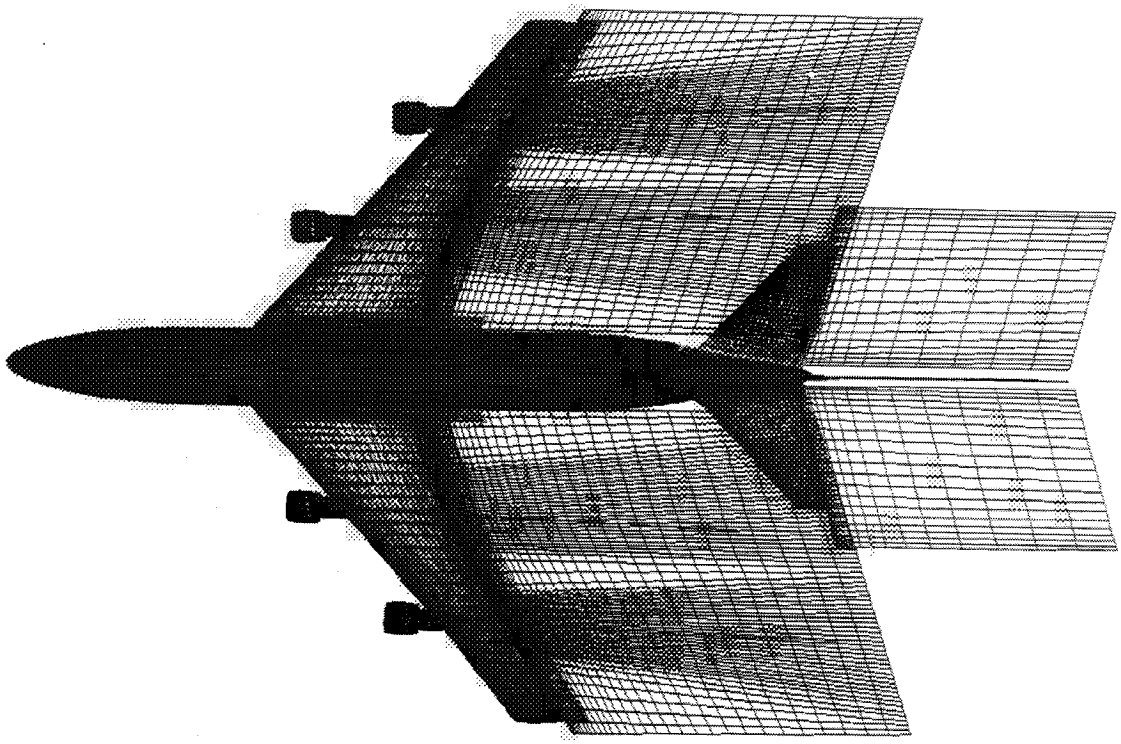

Fig. 3: A view of the overset surface grids for the clean aircraft.

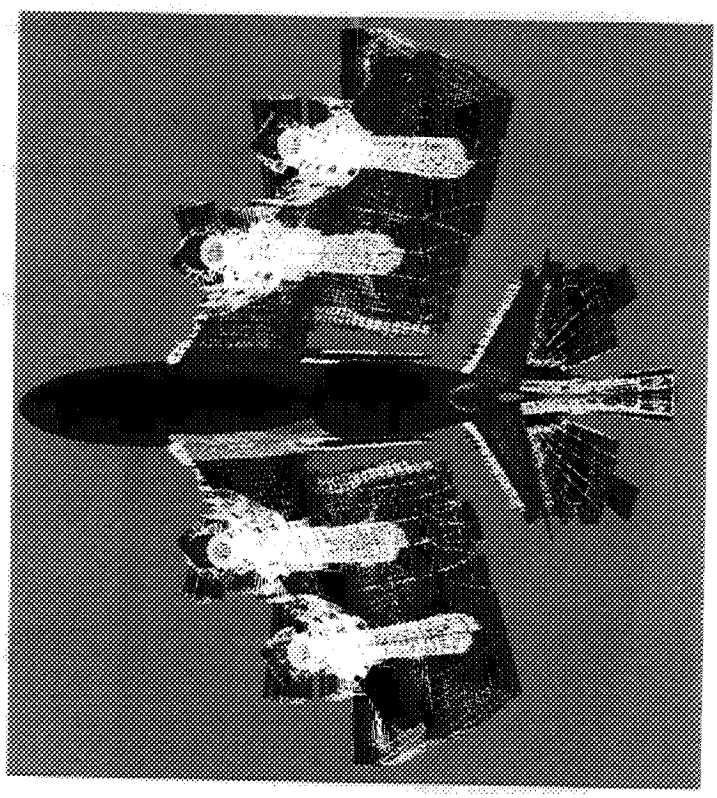

Fig. 4: A view of the hole boundaries in the Chimera grids of clean aircraft generated by the PEGSUS code.

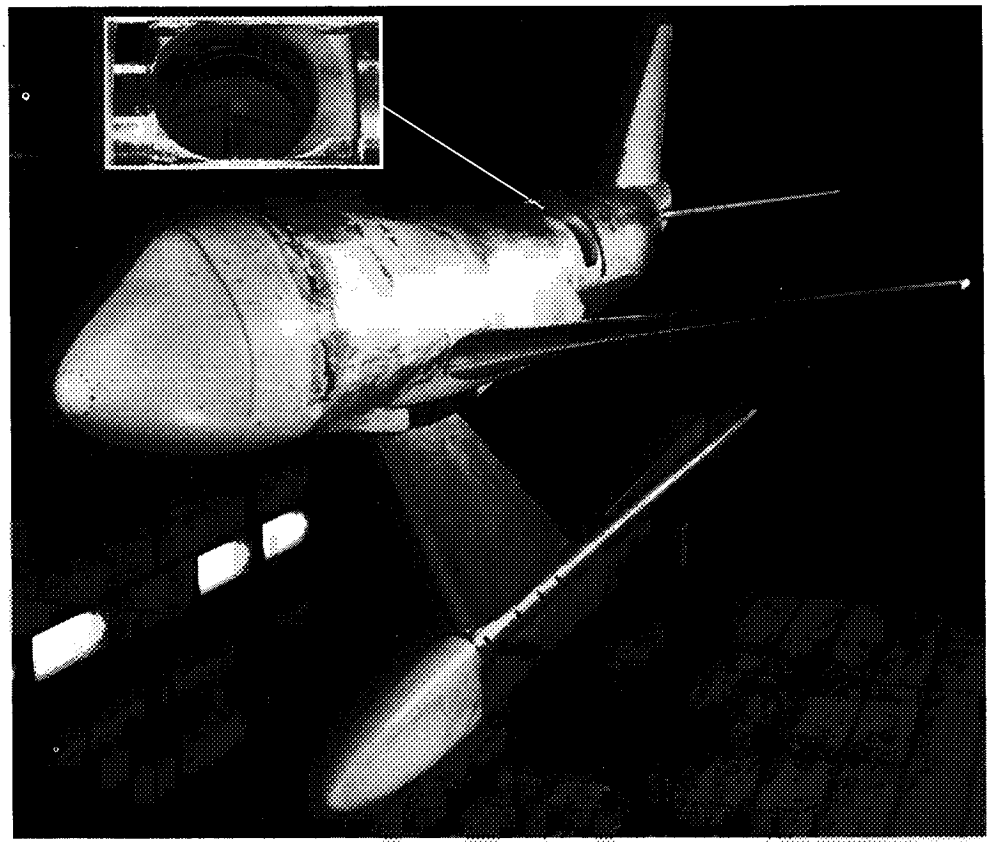

Fig. 5: Wind tunnel 1/7th scale model of the Boeing 747-200 aircraft showing the aft located cavity and telescope.

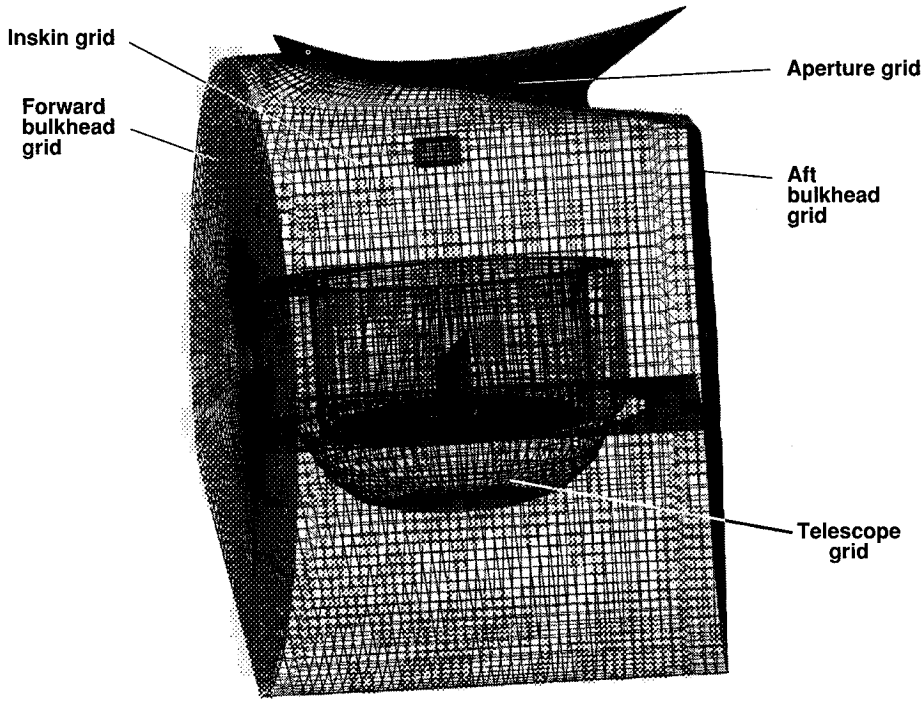

Fig. 6: The details of cavity and telescope surface grids.

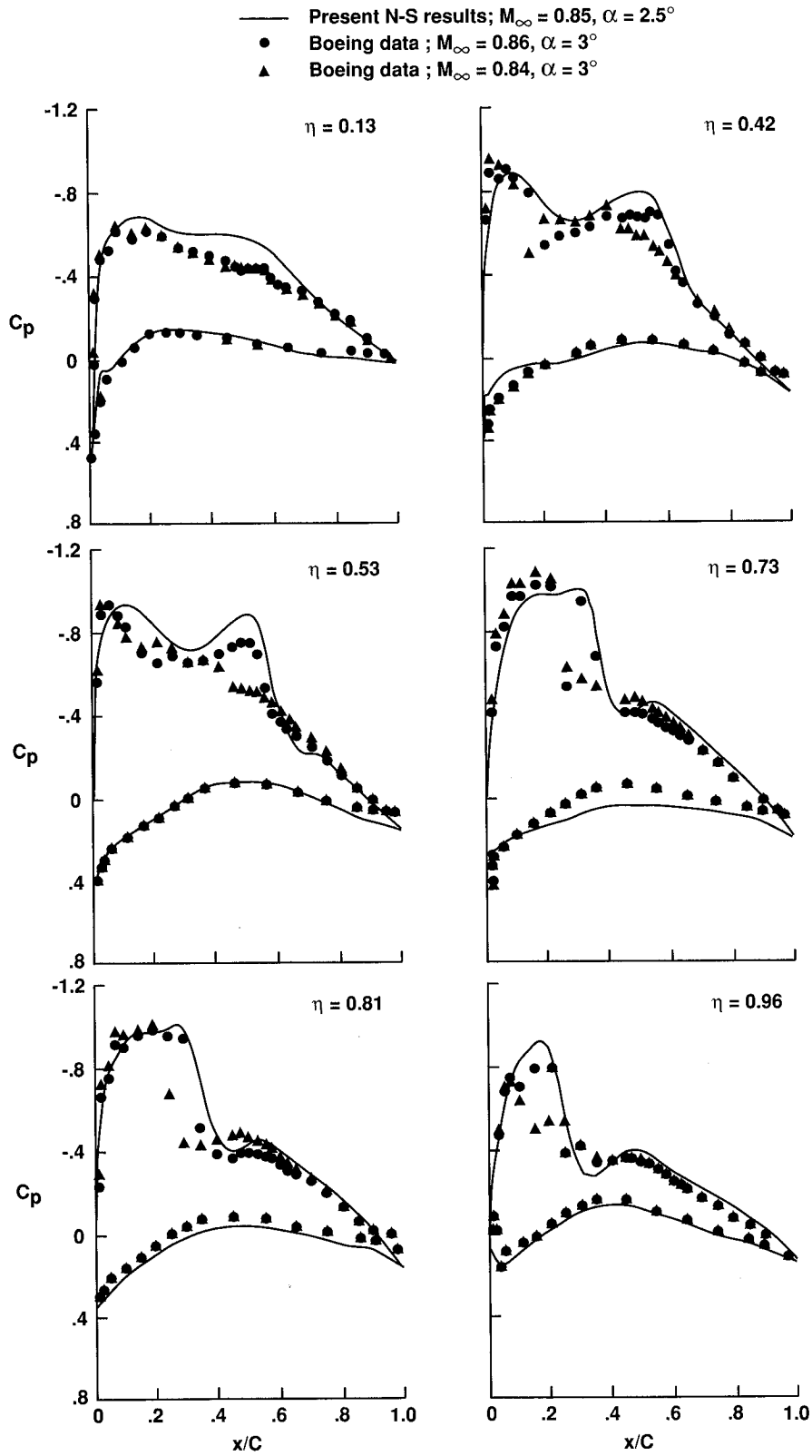

Fig. 7: Steady surface pressure distributions on the wing compared to the experimental data. $M_\infty = 0.85$, $\alpha = 2.5°$, and $Re = 1.85 \times 10^6$. (x is along the chord and C is the local chord.)

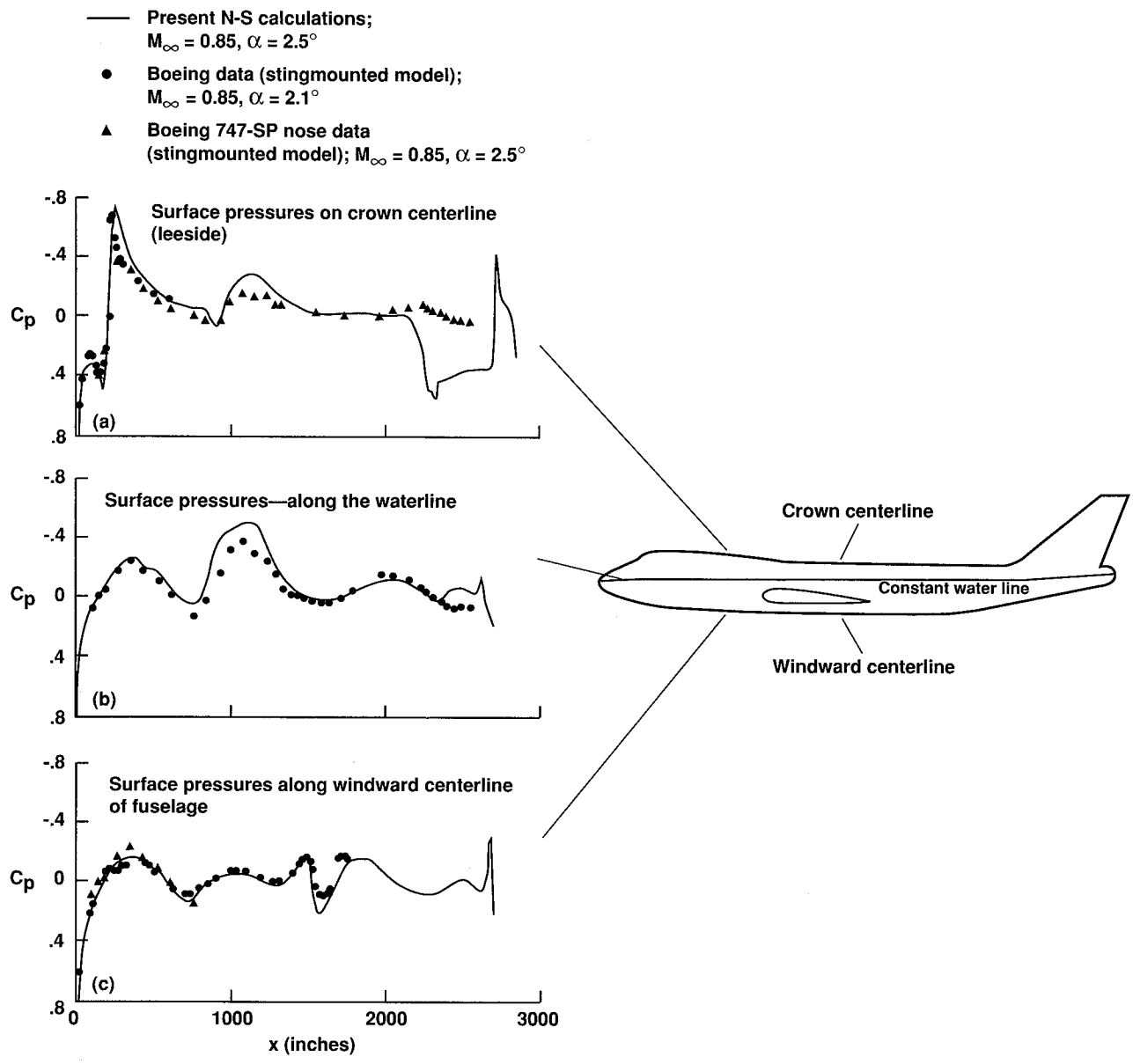

Fig. 8: Steady surface pressure distributions on the fuselage compared to the experimental data. $M_\infty = 0.85$, $\alpha = 2.5°$, and Re = 1.85 x 10^6.

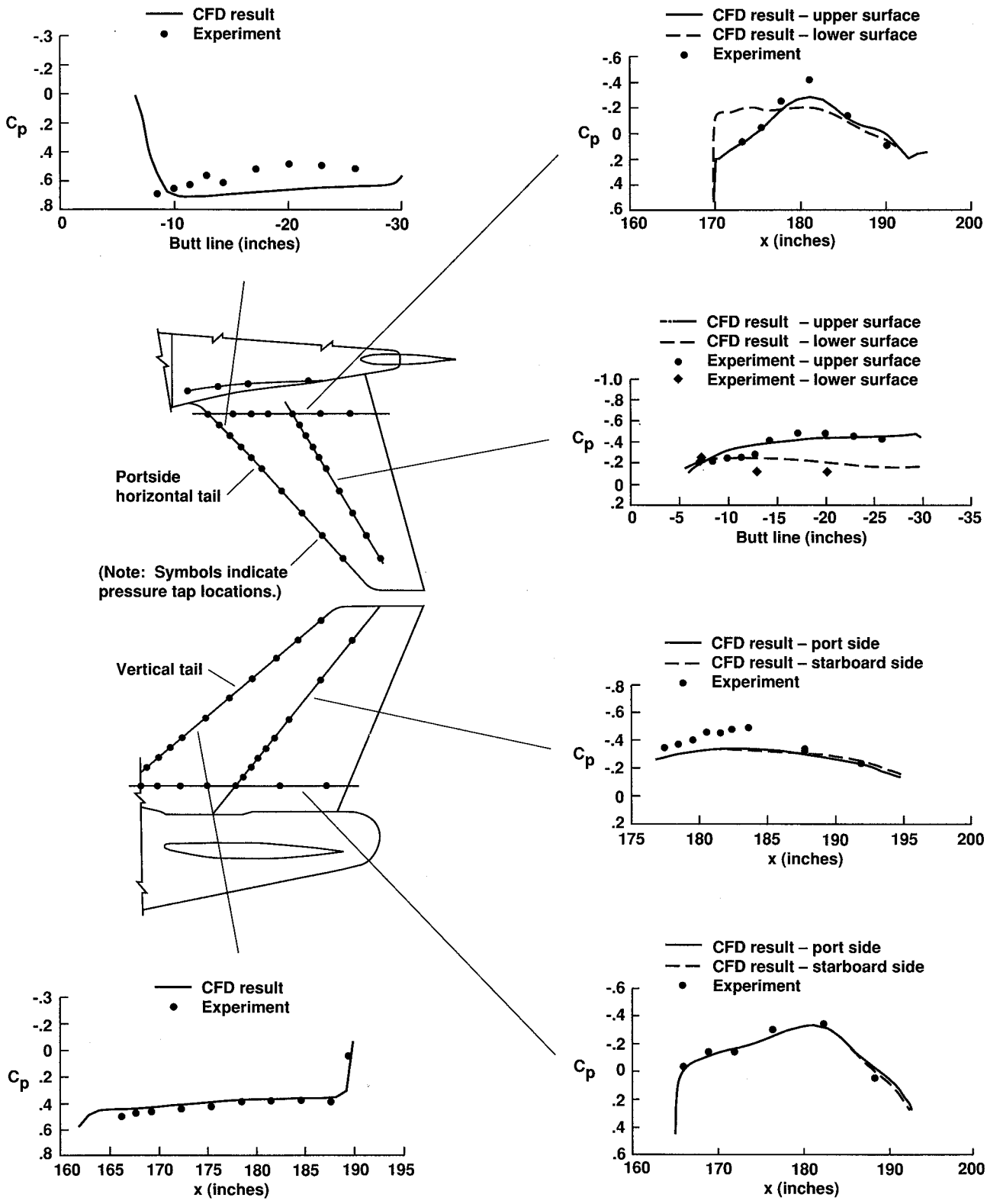

Fig. 9: Comparison of computed and experimental time-averaged surface pressure coefficients on the empennage surfaces at the locations shown.

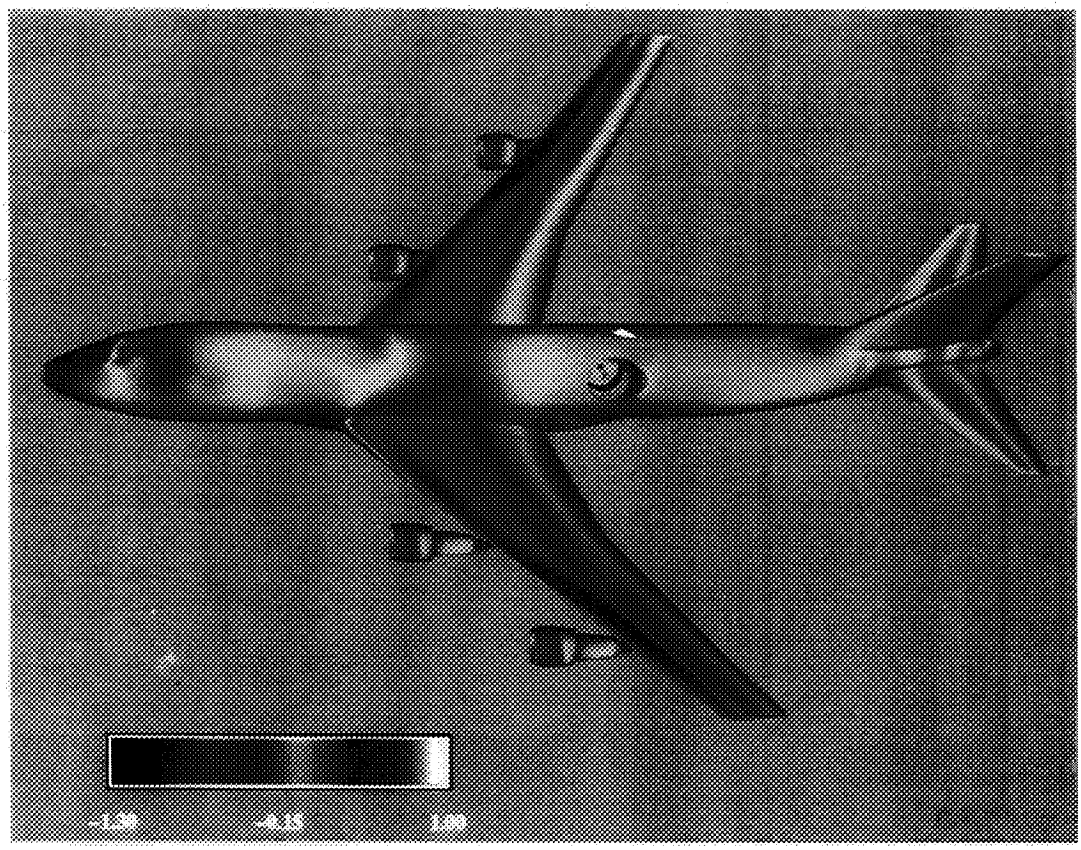

Fig. 10: Instantaneous surface pressure distribution (C_p) at free-flight condition for full configuration aircraft with cavity.

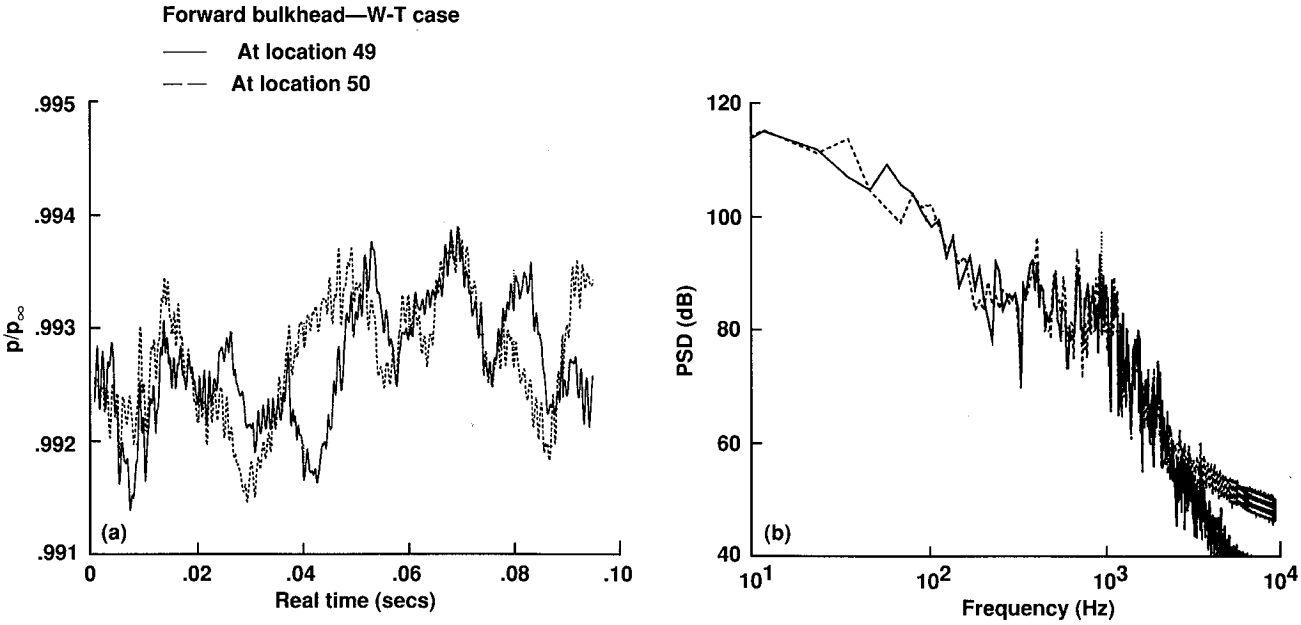

Fig. 11: Unsteady surface pressure histories and PSD computed at wind tunnel conditions for locations shown on forward bulkhead.

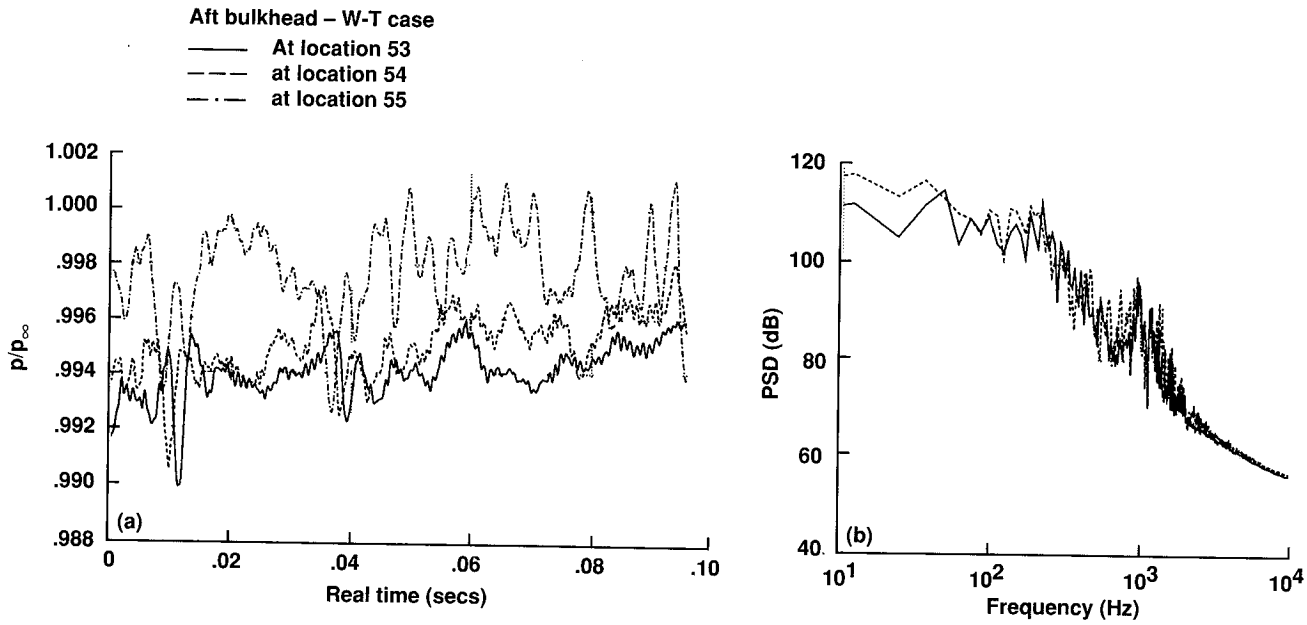

Fig. 12: Unsteady surface pressure histories and PSD computed at wind tunnel condition for locations shown on aft bulkhead.

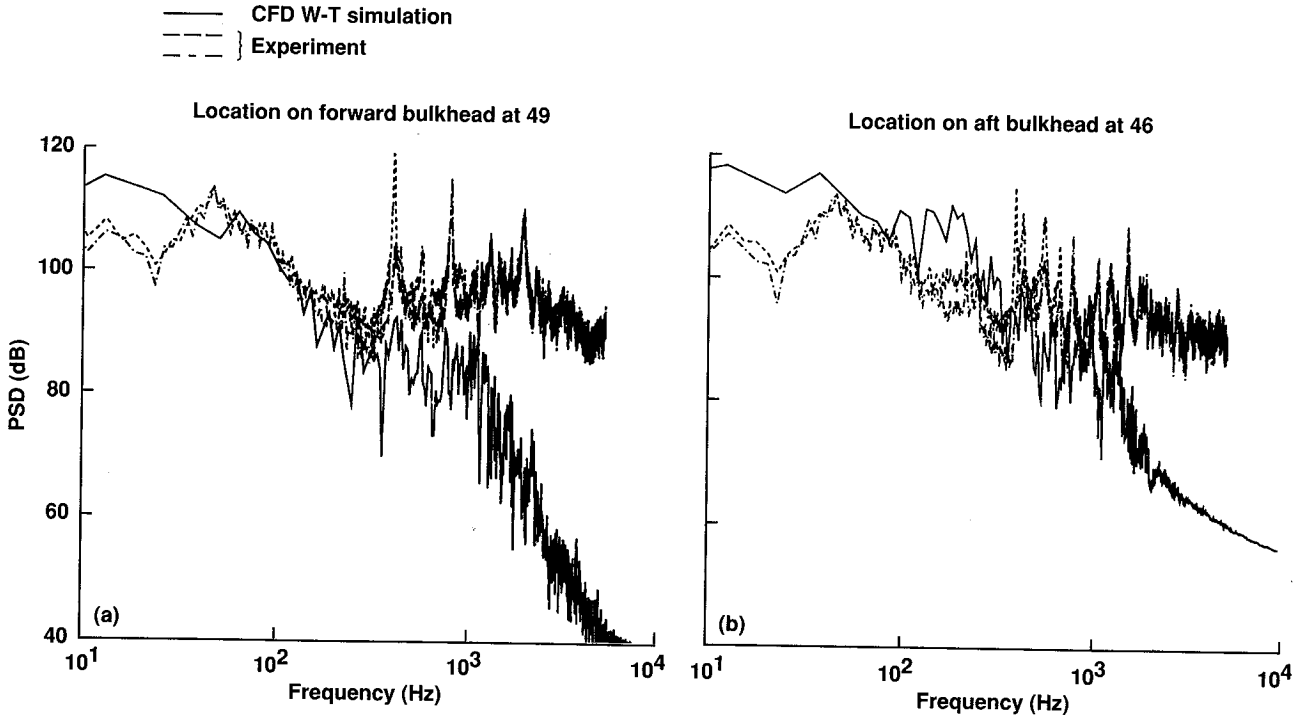

Fig. 13: Comparison of PSD from wind tunnel simulation on bulkhead surface with experimental data.

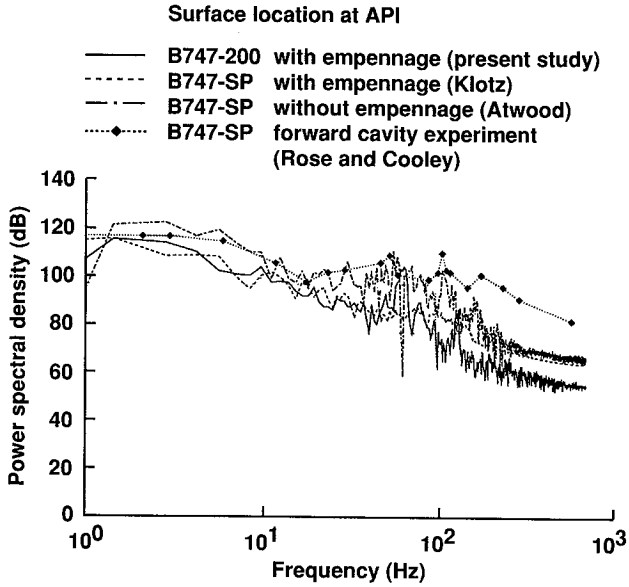

Fig. 14: Power spectra on cavity aperture at location AP1 calculated at free-flight condition for full configuration and scaled to wind tunnel condition and compared with other data.

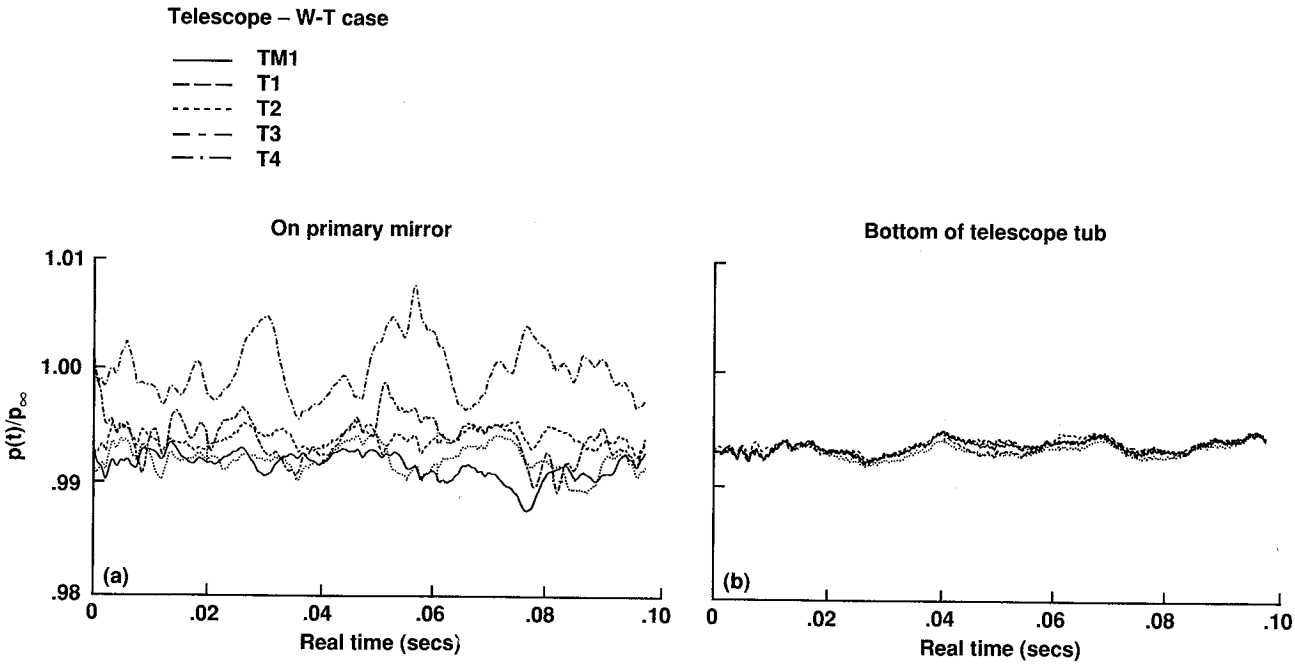

Fig. 15: Unsteady surface pressure histories on the telescope primary mirror and tub at the locations shown.

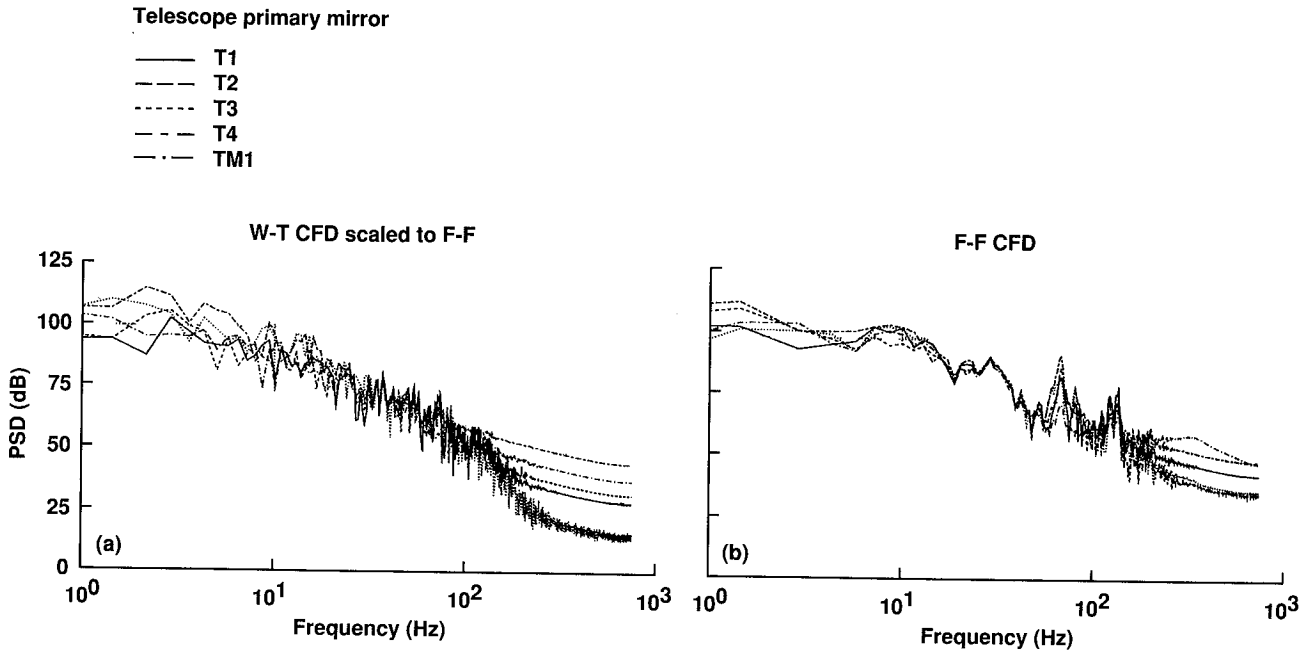

Fig. 16: Power Spectra at specified locations on telescope primary mirror from CFD simulations.

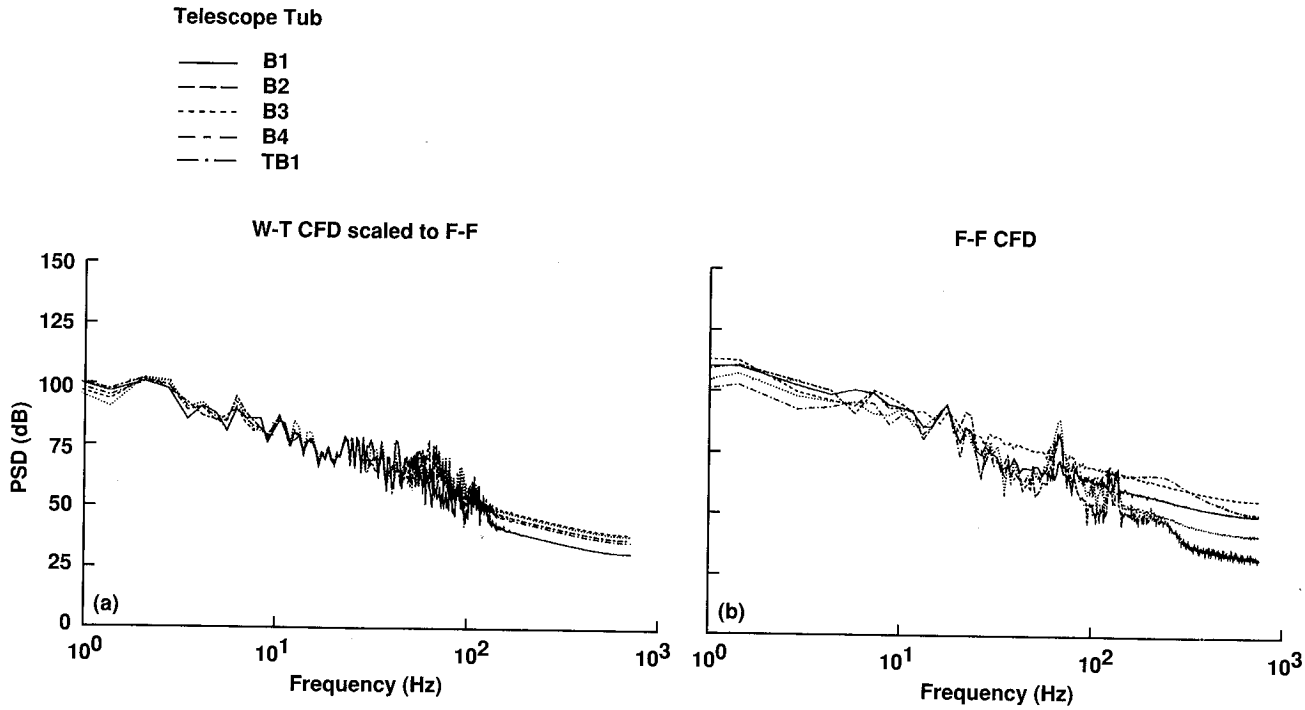

Fig. 17: Power spectra at specified locations on the telescope tub from CFD simulations.

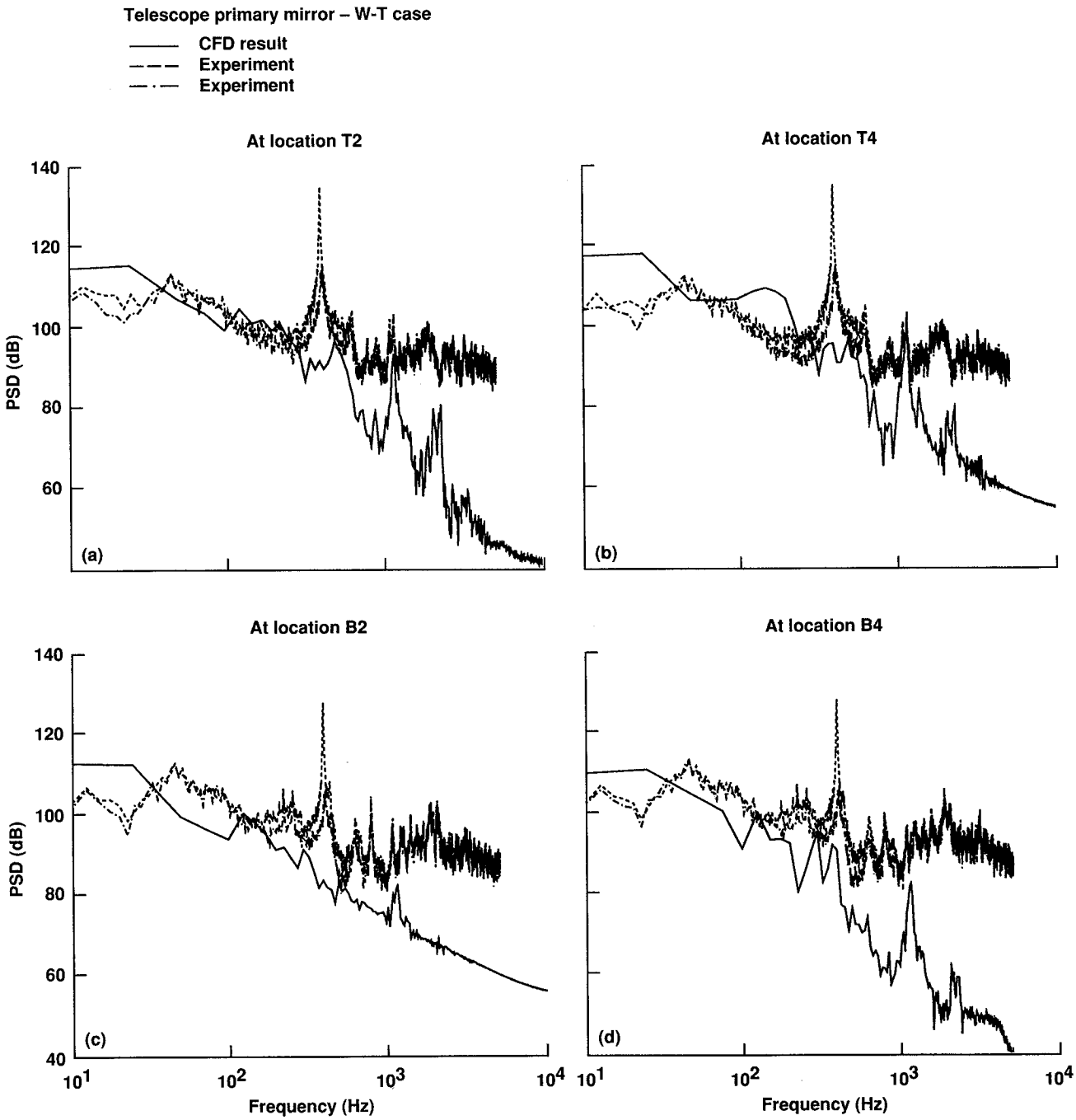

Fig. 18: Comparison of computed PSD at different locations on the telescope primary mirror and tub with experiment.

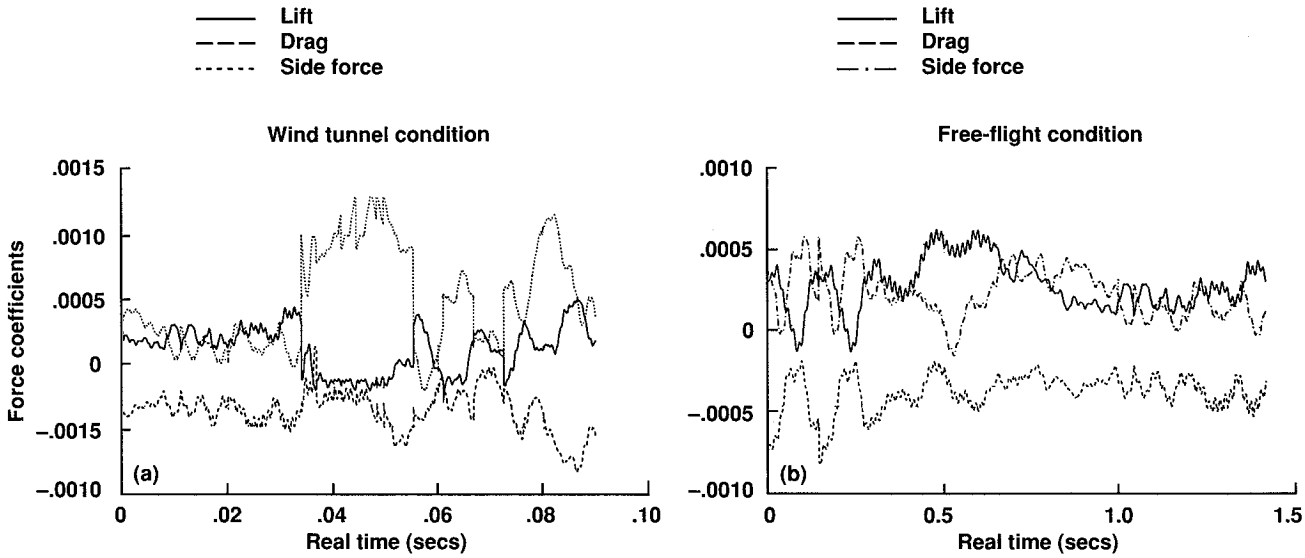

Fig. 19: Time histories of telescope force coefficients from CFD simulations.

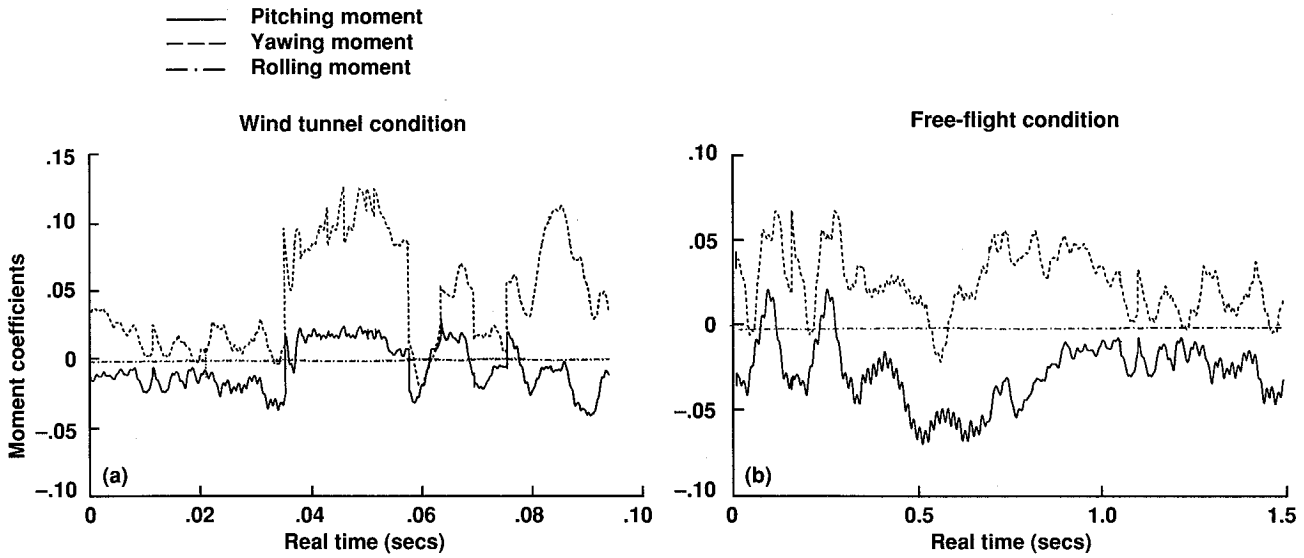

Fig. 20: Time histories of telescope moment coefficients from CFD simulations.

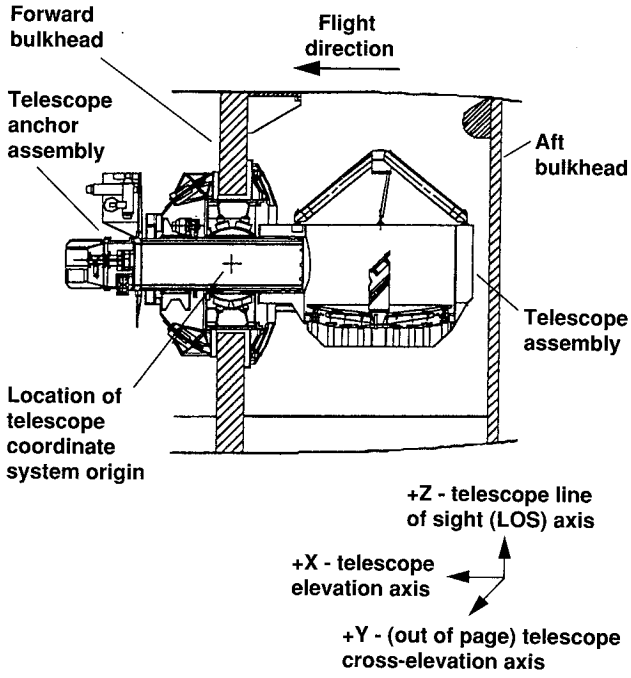

Fig. 21: Telescope coordinate system (fixed to telescope frame of reference).

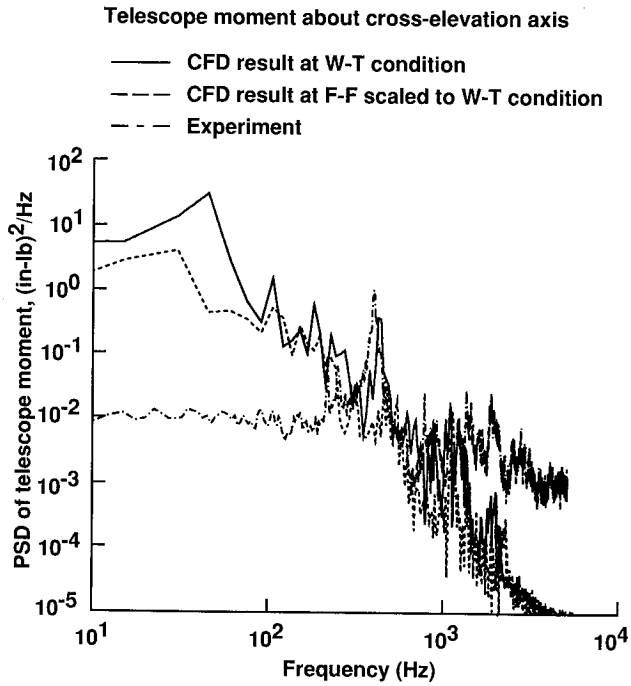

Fig. 22: Comparison of computed and experimental telescope moment about cross-elevation axis at wind tunnel condition.

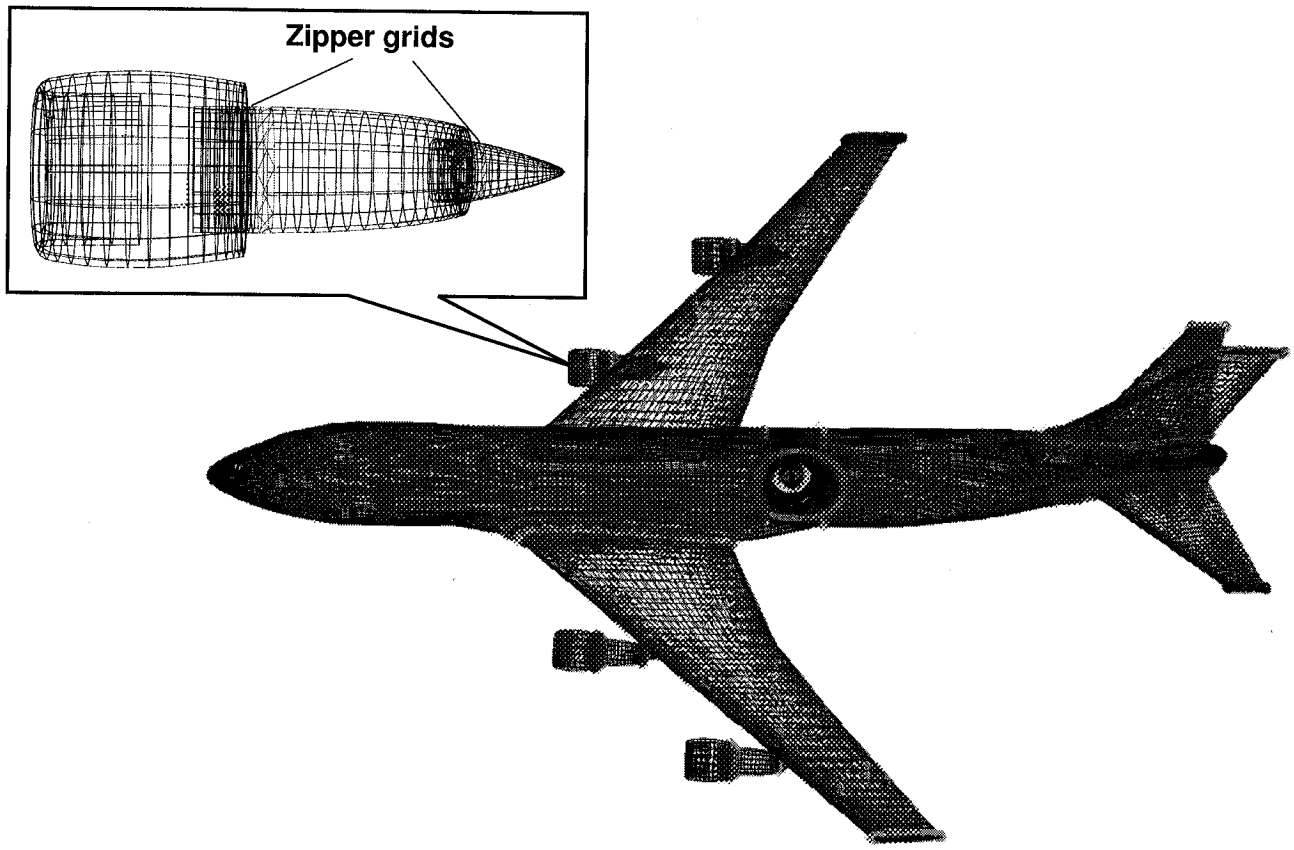

Fig. 23: Location and topology of zipper grids in the overset grid regions for aircraft with cavity.